WATER STRUCTURE

Visualizing Eigen/Zundel cations and their interconversion in monolayer water on metal surfaces

Ye Tian[1]†, Jiani Hong[1]†, Duanyun Cao[2,3]†, Sifan You[4]†, Yizhi Song[1], Bowei Cheng[1], Zhichang Wang[1], Dong Guan[1], Xinmeng Liu[1], Zhengpu Zhao[1], Xin-Zheng Li[5,6,7,8], Li-Mei Xu[1,6,8], Jing Guo[9]*, Ji Chen[5,8]*, En-Ge Wang[1,6,8,10]*, Ying Jiang[1,6,8,11]*

The nature of hydrated proton on solid surfaces is of vital importance in electrochemistry, proton channels, and hydrogen fuel cells but remains unclear because of the lack of atomic-scale characterization. We directly visualized Eigen- and Zundel-type hydrated protons within the hydrogen bonding water network on Au(111) and Pt(111) surfaces, using cryogenic qPlus-based atomic force microscopy under ultrahigh vacuum. We found that the Eigen cations self-assembled into monolayer structures with local order, and the Zundel cations formed long-range ordered structures stabilized by nuclear quantum effects. Two Eigen cations could combine into one Zundel cation accompanied with a simultaneous proton transfer to the surface. Moreover, we revealed that the Zundel configuration was preferred over the Eigen on Pt(111), and such a preference was absent on Au(111).

Hydrated protons are ubiquitous in solutions and involved in a variety of physical, chemical, biological, and energy-related processes (*1*–*9*). The solvation of hydrated proton lies at the heart of acid-base reactions (*10*), enzymatic functions (*11*), proton channels (*12*, *13*), and hydrogen-fuel cells (*7*, *14*). Despite tremendous theoretical and experimental efforts, the nature of hydrated proton in water has been under long-standing and lively debate, mainly because of the lack of comprehensive atomic-level understanding. In particular, the solvation and dynamics of hydrated protons at water-solid interfaces are highly relevant to the key features of electrochemical reactions, such as hydrogen evolution reaction (HER) (*15*, *16*). Whether the hydrated protons are stable and in what forms they exist still remain unclear, hindering a deeper understanding on the detailed reaction pathways on different electrodes (*16*, *17*).

Many different forms of hydrated protons in water have been reported, among which the Zundel cation ($H_5O_2^+$) (*18*) and the Eigen cation ($H_9O_4^+$) (*19*) are the most representative ones. However, the configuration of Zundel and Eigen cations in bulk and interfacial water has been experimentally elusive. Vibrational spectroscopy, which is sensitive to hydrogen (H) bonding strength and dynamics, has been used to identify the molecular structure of hydrated proton (*20*–*24*). Nevertheless, the spectral approach is inefficient because of the transient nature of hydrated protons and extremely diffuse vibrational signatures. Although this problem can be largely avoided for probing protonated gas-phase clusters (*25*–*27*), the obtained knowledge of an isolated cluster is not necessarily applicable to extended H bonding networks and interfacial systems, in which multiple interactions usually compete.

Recently, qPlus-based atomic force microscopy (AFM) (*28*) with a carbon monoxide (CO)–terminated tip has been successfully applied to probe interfacial water and hydrated alkali ions with submolecular resolution in a nearly noninvasive manner (*29*–*31*), on the basis of delicate high-order electrostatic forces. The proton affinity of individual surface hydroxyl was also directly quantified with an OH-terminated tip (*32*). However, imaging and identifying hydrated protons within the H bonding network of water remain a great challenge because of the high similarity between the hydronium (H_3O^+) and the water molecule (H_2O). In this work, we further improved the resolution and sensitivity of the qPlus-AFM [figs. S1 and S2 and supplementary materials (SM)], so that the Zundel and Eigen cations could be directly visualized and distinguished within the monolayer water on metal surfaces at 5 K under ultrahigh vacuum.

Scanning tunneling microscopy (STM) images of the coadsorbed deuterium (D) atoms and D_2O molecules on Au(111) surface are shown in Fig. 1A (SM, materials and methods). The substitution between H and D had a negligible effect on the structures of hydronium-water layers. Most of the results shown in the current work were done with D because of the higher stability of D-doped D_2O layer under the scanning. The D atoms were ionized by transferring electron charge to the Au substrate and water molecules (figs. S3 and S4). The ionized D^+ and D_2O molecules could self-assemble into a two-dimensional (2D) island with a monolayer height (Fig. 1A, bottom right, and fig. S5), which exhibited a honeycomb structure commensurate with the Au(111) lattice (Fig. 1A, bottom left). However, it is challenging to identify hydronium ions (D_3O^+) solvated in the H bonding network of water from the STM images. The height-dependent AFM images and simulations of the 2D hydronium-water structure are shown in Fig. 1, B to D. At the large tip height, the hydronium ions were visualized as individual protrusions with random distribution mainly through the high-order electrostatic force (Fig. 1B, top, and fig. S6) (*29*, *31*). The zoomed-in AFM image clearly indicates that each bright protrusion was surrounded by three symmetric depressions (Fig. 1B, orange dashed curves). Such a feature is consistent with the structure of D_3O^+, in which the negatively charged O and positively charged D yield opposite force contrast. When the tip approached the surface, so that the Pauli repulsive force dominated (*33*, *34*), the bright protrusion evolved into a three-pointed star (Fig. 1C, top). At the smallest tip height, the hexagonal H bonding skeleton of water appeared, and the hydronium ion was imaged as a depression feature owing to the relaxation of the CO tip (Fig. 1D, top).

Although the distribution of hydronium ions has no long-range order, the distance between them was typically 505 and 569 pm, corresponding to the meta-site and the para-site of the hexagonal water ring, respectively (fig. S7). To gain insights into the structure of the solvated hydronium, we constructed a periodic structure that consists of para-hydronium (Fig. 1E). Such a structure was energetically stable (fig. S8) and could be considered as the self-assembly of Eigen cations ($D_9O_4^+$), in which one flat hydronium ion at the center is H bonded with three water molecules (*19*).

[1]International Center for Quantum Materials, School of Physics, Peking University, Beijing 100871, China. [2]Beijing Key Laboratory of Environmental Science and Engineering, School of Materials Science and Engineering, Beijing Institute of Technology, Beijing 100081, China. [3]Beijing Institute of Technology Chongqing Innovation Center, Chongqing 401120, China. [4]Institute of Functional Nano and Soft Materials, Jiangsu Key Laboratory for Carbon-Based Functional Materials and Devices, Soochow University, Suzhou 215123, China. [5]School of Physics, Peking University, Beijing 100871, China. [6]Collaborative Innovation Center of Quantum Matter, Beijing 100871, China. [7]State Key Laboratory for Mesoscopic Physics and Frontiers Science Center for Nano-optoelectronics, School of Physics, Peking University, Beijing 100871, China. [8]Interdisciplinary Institute of Light-Element Quantum Materials and Research Center for Light-Element Advanced Materials, Peking University, Beijing 100871, China. [9]College of Chemistry, Beijing Normal University, Beijing 100875, China. [10]Songshan Lake Materials Lab, Institute of Physics, CAS and School of Physics, Liaoning University, Shenyang 110036, China. [11]CAS Center for Excellence in Topological Quantum Computation, University of Chinese Academy of Sciences, Beijing 100190, China.
***Corresponding author. Email: jguo1294@bnu.edu.cn (J.G.); ji.chen@pku.edu.cn (J.C.); egwang@pku.edu.cn (E.-G.W.); yjiang@pku.edu.cn (Y.J.)**
†These authors contributed equally to this work.

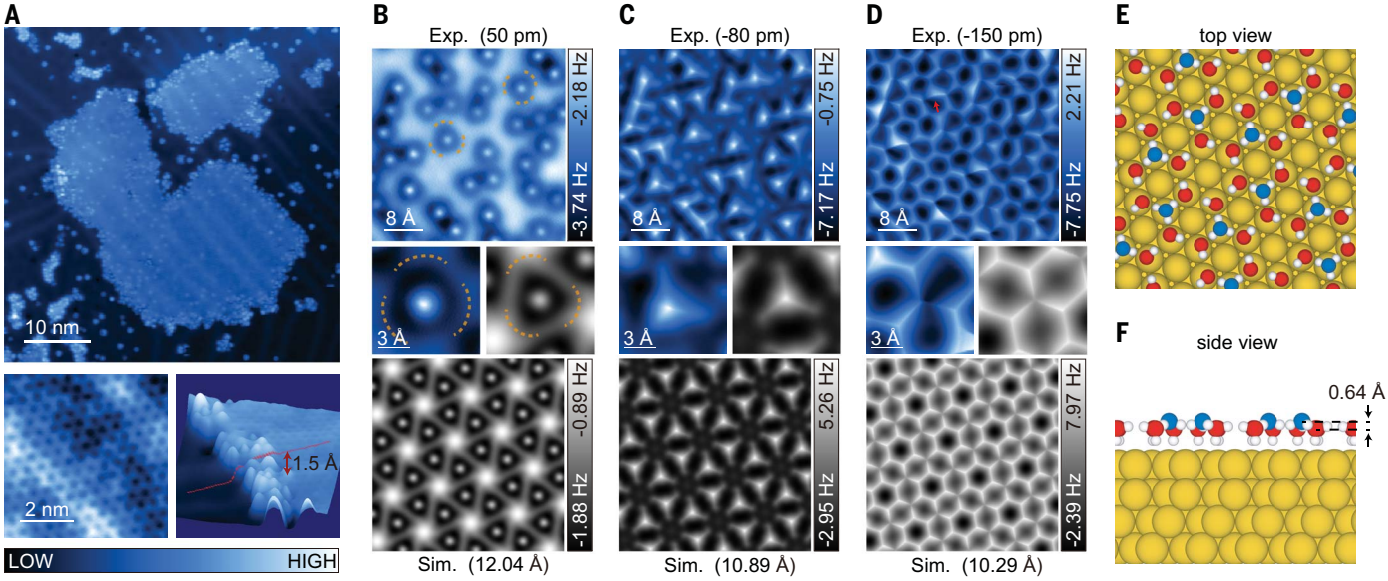

Fig. 1. Atomic structure of self-assembled Eigen-water monolayer on Au(111) surface. (**A**) Overview STM image of the Eigen-water layer formed on Au(111) surface after coadsorption of D atoms and water molecules (D_2O) and subsequently annealing at 120 K. (Bottom) Zoom-in STM images of the hydronium-water island, showing the hexagonal honeycomb structure (left) with the height of ~1.5 Å (right). STM set point, 100 mV and 50 pA. (**B** to **D**) Height-dependent AFM images and simulations of the hydronium-water layer, obtained at the tip heights of (B) (top) 50 pm and (bottom) 12.04 Å, (C) (top) −80 pm and (bottom) 10.89 Å, and (D) (top) −150 pm and (bottom) 10.29 Å. (Middle) Zoom-in AFM images and the simulations of a single Eigen cation in the 2D hydronium-water layer. The yellow dashed curves indicate three symmetric depressions induced by the positively charged hydronium. (**E**) Top and (**F**) side views of the schematic structures of the periodic Eigen-water monolayer with Eigen cations residing at the para-site of the hexagonal water ring. The height difference between hydronium ion and water molecule is indicated in (F). The tip heights in AFM images are referenced to the STM set point on the Eigen-water layer (100 mV and 50 pA). The tip heights in AFM simulations are defined as the vertical distance between the apex atom of the metal tip and the outmost atom of Au substrate. Au, H, and O atoms in the H-down water molecules are indicated with yellow, white, and red spheres, respectively. O atoms in the hydronium are indicated with blue spheres.

Density functional theory (DFT) calculation revealed that the central hydronium ion was ~64 pm higher than the neighboring water molecules, which were in an H-down configuration because of the negatively charged surface (Fig. 1F). The simulated AFM images (Fig. 1, B to D, bottom, and fig. S6) agreed well with the experimental ones (Fig. 1, B to D, top, and fig. S6), further validating the assignment of the Eigen cations. The introduction of meta-hydronium may break the long-range order and led to local defects (Fig. 1D, top, red arrow).

A more ordered structure could form when dosing D at higher coverages (Fig. 2). The STM image (Fig. 2A) showed a similar honeycomb structure as the one in Fig. 1A, but with a larger apparent height (Fig. 2A, bottom right, and fig. S5) and a smaller lattice constant (table S1). The AFM images (Fig. 2, B to D, and fig. S6) at the large and intermediate tip heights exhibit a dimer-like structure with a long-range 3 × 3 periodicity (Fig. 2, B and C, top), with a domain size up to 900 nm^2 (fig. S10). At the smallest tip height, a honeycomb structure was observed (Fig. 2D, top). It is straightforward to infer that such a structure may arise from the dimerization of the ortho-site hydronium ions, so that the two flat water molecules share an extra D^+ in a symmetric H bonding configuration (Fig. 2E), corresponding to the Zundel cation ($D_5O_2^+$) (*18*). The Zundel cation together with four neighboring H-down water molecules formed a basic unit ($D_{13}O_6^+$), which then self-assembled into a perfect 3 × 3 structure (Fig. 2E and fig. S9).

To further explore the stability of the Zundel-water monolayer, we performed detailed path integral molecular dynamics (PIMD) simulations based on DFT calculations, which include the nuclear quantum effects (NQEs) explicitly (SM, materials and methods, and table S2). These results showed that the formation of the Zundel cation was closely related to the NQEs (*1*), which significantly promoted the proton delocalization between the water molecules (Fig. 2E and figs. S11 to S13). The Zundel cation in the configuration based on the PIMD had a ~72 pm larger height than that of the H-down water molecules (Fig. 2F), which is similar to the case of Eigen configuration. The AFM simulation of such a configuration (Fig. 2, B to D, bottom, and fig. S6) nicely reproduced the AFM features observed in the experiment (Fig. 2, B to D, top, and fig. S6). The evidence of the symmetric H bond could be clearly seen in Fig. 2B, in which the depression feature arising from the shared D^+ was located exactly at the center of each dimer (Fig. 2B, middle, red arrows). Without considering the NQEs, the Zundel cation became unstable and relaxed to the Eigen configuration, which showed a distinct asymmetric dimer feature in the AFM simulation (fig. S14). Consequently, the perfect agreement between the experimental results and the simulated AFM images indicated that the resolution of our qPlus-AFM was high enough to distinguish between the Eigen and Zundel cations, in which the position of protons along the H bond only differed by ~0.2 Å.

Although both the Eigen-type ($H_9O_4^+$) and Zundel-type ($H_{13}O_6^+$) clusters are stable species in the gas phase (*26*), their self-assembly at the interface has not been reported before. The lattice constant of the Zundel-water layer is smaller than that of the Eigen-water layer (table S1), suggesting that the inter–Zundel-cluster H bonding strength in the Zundel-water layer should be larger than that in the Eigen-water layer. Such a difference may arise from the stronger intracluster H bonds within the Eigen cluster, which weakened the intercluster H bonds (table S3). We have observed isolated $D_9O_4^+$ clusters on the surface, and isolated $D_{13}O_6^+$ were absent (fig. S15). Furthermore, we

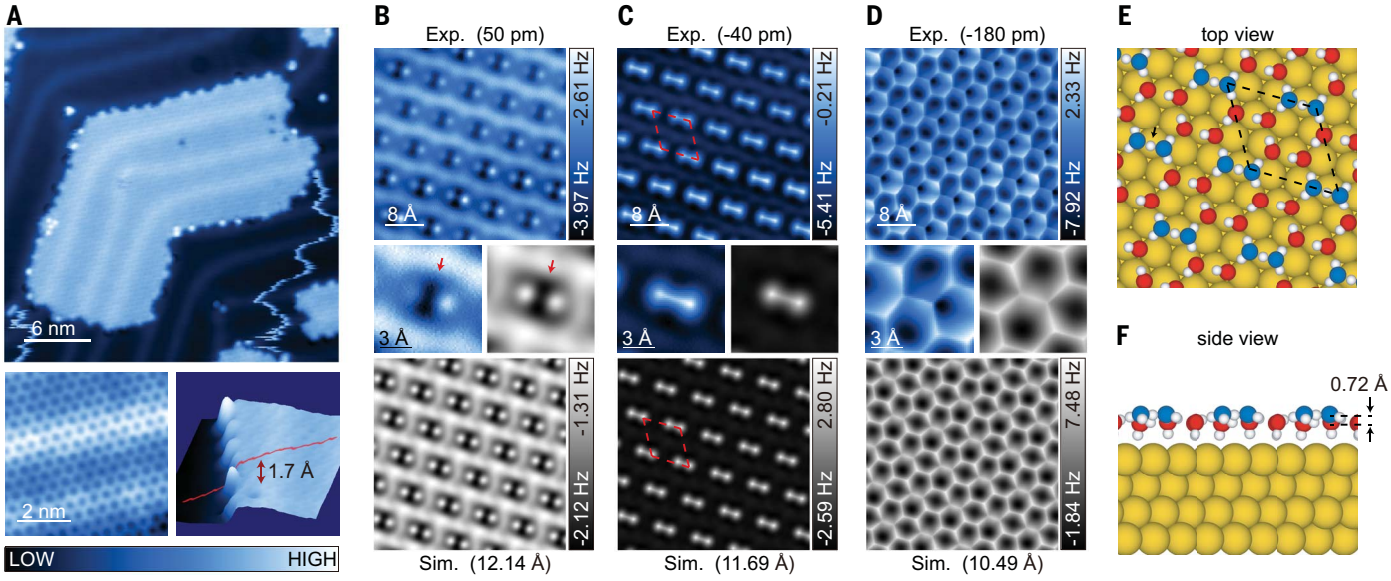

Fig. 2. Atomic structure of self-assembled Zundel-water monolayer on Au(111) surface. (**A**) Overview STM image of the Zundel-water island. (Bottom) Zoom-in STM images, showing the hexagonal honeycomb structure (left) with a height of ~1.7 Å (right). STM set point, 100 mV and 50 pA. (**B** to **D**) Height-dependent AFM images and simulations of the Zundel-water layer, obtained at the tip heights of (B) (top) 50 pm and (bottom) 12.14 Å, (C) (top) −40 pm and (bottom) 11.69 Å, and (D) (top) −180 pm and (bottom) 10.49 Å. (Middle) Zoom-in AFM images and the simulations of a Zundel-type cation in the 2D Zundel-water layer. (**E**) Top and (**F**) side views of the schematic configurations of the Zundel-water layer with a long-range 3 × 3 periodicity obtained with PIMD simulations. The height difference between hydronium ion and water molecule is indicated in (F). The rhombuses in (C) and (E) indicate the 3 × 3 unit cells. The asymmetry of dimers in (B) was caused by the tip asymmetry (fig. S10). The red arrows in (B) indicate the depression feature at the center of each dimer. The black arrow in (E) indicates the shared proton in the Zundel cation. The tip heights in AFM images are referenced to the STM set point on the Zundel-water layer (100 mV and 50 pA). The tip heights in AFM simulations have the same reference and definition as shown in Fig. 1. Au, H, and O atoms in the H-down water molecules are indicated with yellow, white, and red spheres, respectively. O atoms in the Zundel cation are indicated with blue spheres.

found that the interaction between the Zundel-water layer and substrate was weaker than that with the Eigen-water layer (table S3), which was consistent with the observed larger height of the Zundel-water layer (Figs. 1A and 2A and fig. S5). The height difference may result from the weaker inter-Eigen H bonds and the larger density of hydronium in the Eigen-water layer, which could cause a stronger electrostatic attraction between the Eigen-water layer and the substrate (fig. S4 and table S3).

To explore the dynamics of hydronium ions at the interface, which is essential for understanding the HER process (*35*), tip manipulation experiments were carefully performed. The interconversion between the Eigen and Zundel cations induced by the tip is shown in Fig. 3. We applied a voltage pulse on one Zundel cation in the 3 × 3 structure (Fig. 3, A and B, dashed ellipse), leading to the formation of two Eigen cations at the meta-sites (Fig. 3, D and E). The water molecules shared by two hydronium ions after the conversion are indicated with arrows in Fig. 3, E and F. In particular, the water molecule (Fig. 3, E and F, yellow arrow) formed a Bjerrum D-type defect with the neighboring water molecule, whose apparent bond length (300 pm) is larger than that of the intact H bonds (280 pm) (*36*). Those water molecules showed different features from the others, which could be reproduced well with AFM simulation (fig. S16). By applying another voltage pulse, the two Eigen cations could convert back to the Zundel cation.

The interconversion between two Eigen cations and one Zundel cation could only be possible when the D^+ transfer occurred not only between the water molecules but also between the water layer and the surface (Fig. 3, G and H). As voltage pulses were applied, the D-down water molecule shared by the two Eigen cations transferred the downward D^+ to the surface and simultaneously accepted the D^+ transferred from the adjacent hydronium, leading to a flat-lying water molecule and an adsorbed D atom on the surface (D*). Then, the flat water molecule accepted a D^+ from the other adjacent hydronium and formed a symmetric H bond, finally resulting in a stable Zundel+D* configuration (figs. S17 and S18). This conversion from two Eigen cations to the Zundel+D* could be also evidenced in the temperature-dependent experiments (fig. S19). We found that an Eigen cation could neither convert to a Zundel cation without involving interfacial proton transfer nor donate its extra proton to the surface without the help of an additional Eigen cation (fig. S18). Therefore, the formation of Zundel cation and interfacial proton transfer were always coupled together. Such a process (from two Eigens to Zundel+D*) actually corresponds to a previously unknown pathway of Volmer step in HER (*37*), which may greatly facilitate the subsequent Heyrovsky reaction (*38*).

To explore how general those results obtained on Au(111) could be, we performed similar investigations on Pt(111), which is more reactive and hydrophilic than Au(111). It is well known that water forms a $\sqrt{37} \times \sqrt{37}$ monolayer on Pt(111) (*39*, *40*), consisting of pentagons, hexagons, and heptagons (Fig. 4A). When the dosed D coverage was low, individual Zundel cations appeared locally in the $\sqrt{37} \times \sqrt{37}$ phase (Fig. 4D, red arrows). As the D coverage increased, the $\sqrt{37} \times \sqrt{37}$ phase gradually transformed into a $\sqrt{57} \times \sqrt{57}$ phase (Fig. 4B), and the density of Zundel cation also increased, accompanied with the occasional appearance of Eigen cation (Fig. 4E, yellow arrows). The $\sqrt{57} \times \sqrt{57}$ phase finally changed to a honeycomb structure at high D coverages (Fig. 4C), where the Zundel cations formed multiple 3 × 3 domains and the Eigen cations

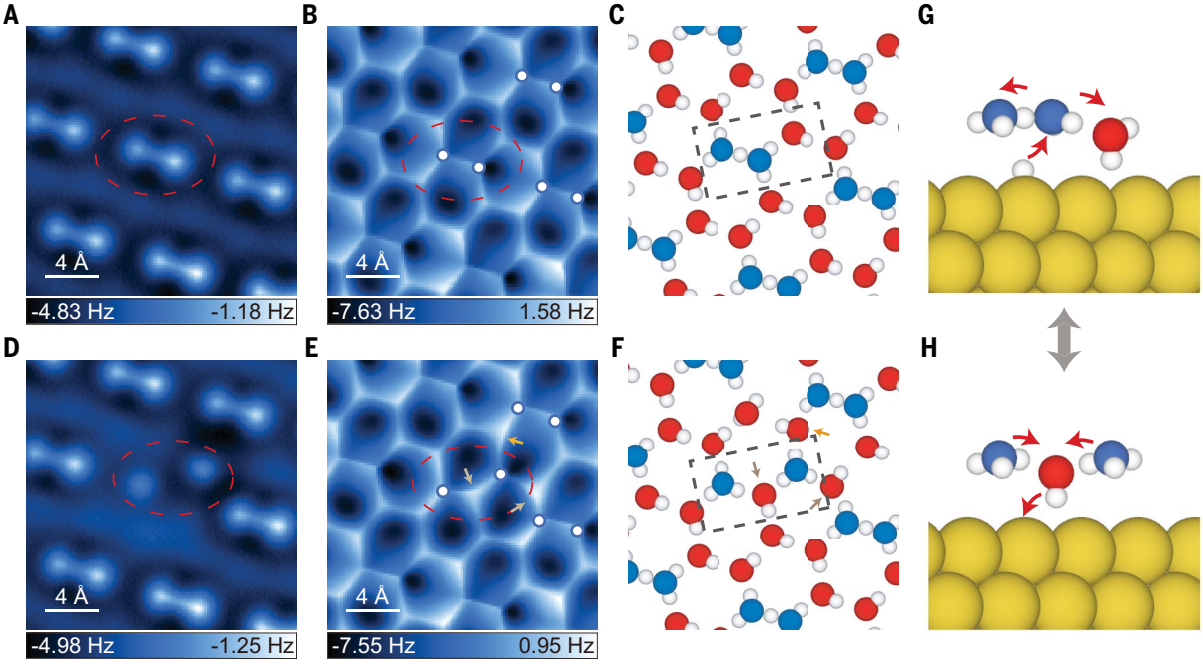

Fig. 3. Tip-induced interconversion between the Eigen and Zundel cations. (**A** to **F**) [(A), (B), (D), and (E)] Height-dependent AFM images and [(C) and (F)] the schematic H-bonding arrangements of [(A) to (C)] the ordered Zundel cations and [(D) to (F)] the tip-induced Eigen cations in the hydronium-water layer. Experimental AFM images were recorded at the tip heights of [(A) and (D)] −50 pm and [(B) and (E)] −180 pm. The red dashed ellipses in (A), (B), (D), and (E) and the black dashed rectangles in (C) and (F) indicate the transition from a Zundel cation (dimer) to two Eigen cations (monomer). The gray and yellow arrows in (E) indicate the AFM features induced by the H-down water molecules shared by the hydroniums at the meta-sites [(F), gray arrows] and the one at the Bjerrum D-type defect [(F), yellow arrow], respectively. (**G** and **H**) Schematic models of the interconversion between the Zundel-type and Eigen-type cations. Au, H, and O atoms in the H-down water molecules are indicated with yellow, white, and red spheres, respectively. O atoms in the Zundel and Eigen cations are indicated with blue spheres. The red arrows indicate the proton transfer pathway during the transition. The tip heights in AFM images are referenced to the STM set point on the Zundel-water layer (100 mV and 50 pA).

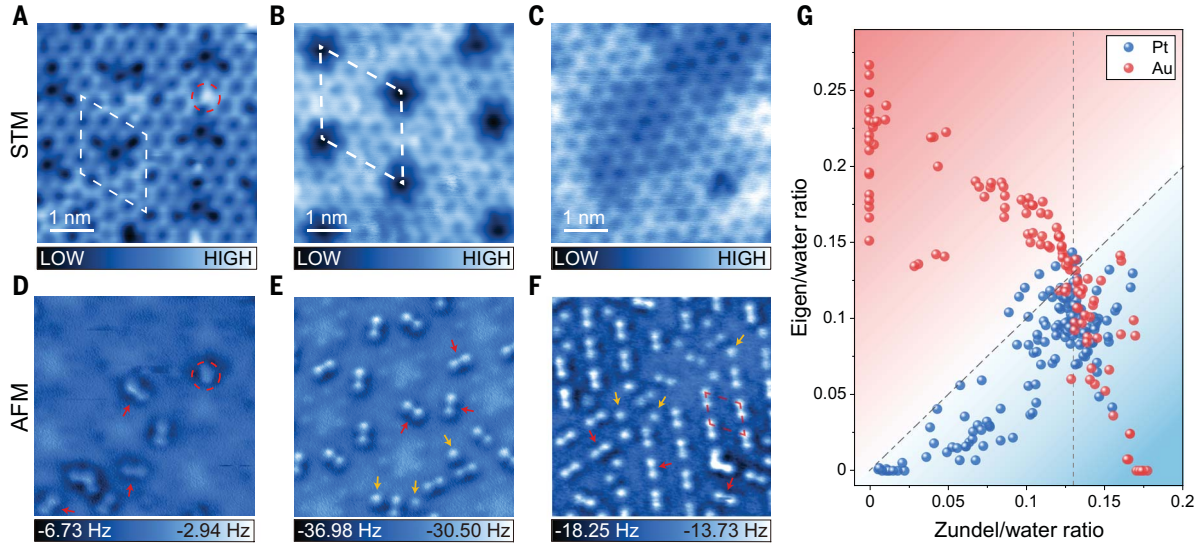

Fig. 4. Hydronium-water overlayer on Pt(111) surface. (**A** to **C**) STM topography and (**D** to **F**) the corresponding AFM images of the hydronium-water overlayer on Pt(111) surface obtained with increasing D coverages. The rhombuses in (A), (B), and (F) indicate the $\sqrt{37} \times \sqrt{37}$, $\sqrt{57} \times \sqrt{57}$, and 3 × 3 unit cells, respectively. STM set points on Pt(111) are (A) 100 mV and 20 pA, (B) 100 mV and 50 pA, and (C) 50 mV and 40 pA. Experimental Δf images were recorded at the tip heights of (D) 80 pm, (E) 100 pm, and (F) 0 pm, respectively. In (D) to (F), the red and yellow arrows indicate the dimer and monomer features, respectively, corresponding to the Zundel- and Eigen-type cations. In (A) and (D), the red dashed circles indicate the D-up water molecule, showing as bright protrusions in both STM and AFM images. (**G**) Density correlation between the Eigen and Zundel on the Au(111) and Pt(111) surfaces at different proton/water ratios (0.01 to 0.45) and different annealing temperature (110 to 145 K), obtained from 35 different samples for Au(111) and 30 different samples for Pt(111). The red and blue shaded areas indicate Eigen- and Zundel-dominant regions, respectively. The vertical dashed line indicates where the Zundel/water ratio equals to 0.13. The diagonal dashed line indicates where the ratios of Zundel/water and Eigen/water are equal.

mainly located at the domain boundaries (Fig. 4F and figs. S20 and S21). We could also achieve the interconversion between two Eigen cations and one Zundel cation on Pt(111) through tip manipulation (fig. S22), suggesting that there was a D* under the Zundel cation (Zundel+D*).

Although the Eigen and Zundel cations could form the similar monolayer structure on Pt(111) and Au(111), there are still some differences between these two surfaces. In Fig. 4G, we plot the density correlation between the Eigen and Zundel cations (figs. S21 and S23), in which two main features could be identified. First, there was a clear transition from the Eigen to Zundel structure on Au(111), and the Zundel was always preferred on Pt(111). The density correlation followed the same behavior for both surfaces when the ratio of Zundel/water was larger than 0.13. Second, the Eigen and Zundel structures could exist even at very low densities on Pt(111), and for Au(111), a minimum density of Eigen and Zundel was needed to stabilize the monolayer. Those distinct features could be understood through the theoretical analysis of thermodynamic stability of the Eigen and Zundel phases in terms of the H chemical potential, which shows that the transition point from the Eigen phase to the Zundel phase on Pt(111) shifts to considerably lower H potential than that on Au(111) (fig. S24). The lattice constant of Pt(111) is smaller than that of the Au(111), thus favoring the delocalization of the extra proton between the water molecules and stabilizing Zundel over Eigen (table S1). The preference of Zundel+D* configuration on Pt(111) could be also related to the stronger Pt-D interaction. In addition, the stronger interaction between the Pt(111) and water could help to stabilize the hydrated protons at small densities.

Our results may provide new insights into the different reaction kinetics of HER on Au(111) and Pt(111) surfaces. On Au(111), the Eigen configuration was dominant, and the Zundel only appeared when the Eigen density became sufficiently large, and the Zundel configuration was always preferred on Pt(111) regardless of the proton density. This suggested that distant hydrated protons were more inclined to combine on Pt(111), thus facilitating the production of H_2. At low Zundel density, the Zundel+H* configuration on Pt(111) may allow efficient H_2 evolution through the Heyrovsky reaction pathway. However, at high Zundel density, the coverage of H* on the Pt(111) was also increased, which promoted the Tafel reaction pathway (*41*, *42*). This feature may provide microscopic insights into the behavior of reaction kinetics on Pt(111) as changing the electrochemical potential (the proton density near the surface) (*43*).

The formation of stable Eigen and Zundel cations is expected to be general on other noble metal surfaces with different reactivity. We have observed similar Eigen and Zundel structures on Ru(0001) and Cu(111) surfaces (figs. S25 and S26). Our PIMD simulations showed that the Zundel and Eigen structures observed in this work remained stable even up to room temperature despite thermal broadening (fig. S13). Further considering that the water layers near the liquid-solid interface can be relatively ordered (ice-like) because of the prominent metal-water interaction (*44*), especially when the electric potential is applied on the electrode (*45*), the low-temperature water monolayers on metal surfaces studied in this work may provide useful atomic-scale information to understand various electrode processes in aqueous environments. The coupled Eigen-Zundel interconversion and interfacial proton transfer are beyond the known elementary steps for H_2 production, which may help to boost the HER efficiency from a new perspective.

REFERENCES AND NOTES

1. D. Marx, M. E. Tuckerman, J. Hutter, M. Parrinello, *Nature* **397**, 601–604 (1999).
2. N. Agmon *et al*., *Chem. Rev.* **116**, 7642–7672 (2016).
3. K.-D. Kreuer, *Chem. Mater.* **8**, 610–641 (1996).
4. C. A. Wraight, *Biochim. Biophys. Acta Bioenerg.* **1757**, 886–912 (2006).
5. G. A. Voth, *Acc. Chem. Res.* **39**, 143–150 (2006).
6. M. Chen *et al*., *Nat. Chem.* **10**, 413–419 (2018).
7. S. J. Peighambardoust, S. Rowshanzamir, M. Amjadi, *Int. J. Hydrogen Energy* **35**, 9349–9384 (2010).
8. K.-D. Kreuer, S. J. Paddison, E. Spohr, M. Schuster, *Chem. Rev.* **104**, 4637–4678 (2004).
9. D. Marx, *ChemPhysChem* **7**, 1848–1870 (2006).
10. O. F. Mohammed, D. Pines, J. Dreyer, E. Pines, E. T. J. Nibbering, *Science* **310**, 83–86 (2005).
11. M. Garcia-Viloca, J. Gao, M. Karplus, D. G. Truhlar, *Science* **303**, 186–195 (2004).
12. I. S. Ramsey, M. M. Moran, J. A. Chong, D. E. Clapham, *Nature* **440**, 1213–1216 (2006).
13. M. Sasaki, M. Takagi, Y. Okamura, *Science* **312**, 589–592 (2006).
14. T. E. Springer, T. A. Zawodzinski, S. Gottesfeld, *J. Electrochem. Soc.* **138**, 2334–2342 (1991).
15. A. J. Bard, L. R. Faulkner, *Electrochemical Methods: Fundamentals and Applications* (Wiley, ed. 2, 2010).
16. W. Schmickler, E. Santos, *Interfacial Electrochemistry* (Springer, ed. 2, 2010).
17. Y. Kim, S. Shin, H. Kang, *Angew. Chem. Int. Ed.* **54**, 7626–7630 (2015).
18. G. Zundel, H. Metzger, *Z. Phys. Chem.* **58**, 225–245 (1968).
19. E. Wicke, M. Eigen, T. Ackermann, Eds., *Z. Phys. Chem* **1**, 340–364 (1954).
20. M. Thämer, L. De Marco, K. Ramasesha, A. Mandal, A. Tokmakoff, *Science* **350**, 78–82 (2015).
21. F. Dahms, B. P. Fingerhut, E. T. J. Nibbering, E. Pines, T. Elsaesser, *Science* **357**, 491–495 (2017).
22. J. A. Fournier, W. B. Carpenter, N. H. C. Lewis, A. Tokmakoff, *Nat. Chem.* **10**, 932–937 (2018).
23. C. Radüge, V. Pflumio, Y. R. Shen, *Chem. Phys. Lett.* **274**, 140–144 (1997).
24. S. Das, M. Bonn, E. H. G. Backus, *Angew. Chem. Int. Ed.* **58**, 15636–15639 (2019).
25. K. R. Asmis *et al*., *Science* **299**, 1375–1377 (2003).
26. J. M. Headrick *et al*., *Science* **308**, 1765–1769 (2005).
27. J. W. Shin *et al*., *Science* **304**, 1137–1140 (2004).
28. F. J. Giessibl, *Rev. Sci. Instrum.* **90**, 011101 (2019).
29. J. Peng *et al*., *Nat. Commun.* **9**, 122 (2018).
30. R. Ma *et al*., *Nature* **577**, 60–63 (2020).
31. J. Peng *et al*., *Nature* **557**, 701–705 (2018).
32. M. Wagner, B. Meyer, M. Setvin, M. Schmid, U. Diebold, *Nature* **592**, 722–725 (2021).
33. L. Gross, F. Mohn, N. Moll, P. Liljeroth, G. Meyer, *Science* **325**, 1110–1114 (2009).
34. P. Hapala *et al*., *Phys. Rev. B Condens. Matter Mater. Phys.* **90**, 085421 (2014).
35. E. Skúlason *et al*., *Phys. Chem. Chem. Phys.* **9**, 3241–3250 (2007).
36. N. Bjerrum, *Science* **115**, 385–390 (1952).
37. T. Erdey-Grúz, M. Volmer, *Z. Phys. Chem.* **150A**, 203–213 (1930).
38. J. Heyrovský, *Recl. Trav. Chim. Pays Bas* **46**, 582–585 (1927).
39. A. Glebov, A. P. Graham, A. Menzel, J. P. Toennies, *J. Chem. Phys.* **106**, 9382–9385 (1997).
40. S. Nie, P. J. Feibelman, N. C. Bartelt, K. Thürmer, *Phys. Rev. Lett.* **105**, 026102 (2010).
41. J. Tafel, *Z. Phys. Chem.* **50U**, 641–712 (1905).
42. P. S. Rice, Z. P. Liu, P. Hu, *J. Phys. Chem. Lett.* **12**, 10637–10645 (2021).
43. N. M. Marković, B. N. Grgur, P. N. Ross, *J. Phys. Chem. B* **101**, 5405–5413 (1997).
44. T. Fukuma, Y. Ueda, S. Yoshioka, H. Asakawa, *Phys. Rev. Lett.* **104**, 016101 (2010).
45. C. Y. Li *et al*., *Nat. Mater.* **18**, 697–701 (2019).
46. Y. Tian *et al*., Zenodo (2022).

ACKNOWLEDGMENTS

The authors thank the computational resources provided by the TianHe-1A, TianHe II supercomputer, High-performance Computing Platform of Peking University. **Funding:** This work was supported by the National Key R&D Program under grants 2021YFA1400500, 2021YFA1400501, and 2017YFA0205003; the National Natural Science Foundation of China under grants 11888101, 11634001, 21725302, 21902013, 91961118, 11934003, and 11974024; the Strategic Priority Research Program of Chinese Academy of Sciences under grants XDB28000000 and XDB33000000; the Fundamental Research Funds for the Central Universities, Beijing Municipal Science and Technology Commission under grant Z181100004218006; the Beijing Natural Science Foundation under grant 1202016; the National Postdoctoral Program for Innovative Talents under grant BX2021040; and the China Postdoctoral Science Foundation under grant 2021M690408. **Author contributions:** Conceptualization and supervision: Y.J. and E.-G.W.; STM/AFM measurements: Y.T., J.H., J.G., S.Y., Z.W., D.G., X.L., Z.Z., and B.C.; Ab initio DFT calculations and AFM simulations: D.C., Y.S., and L.-M.X.; PIMD simulations: J.C. and X.-Z.L.; Interpretation of the data: Y.J., E.-G.W., J.C., J.G., L.-M.X., X.-Z.L, Y.T., D.C., J.H., Y.S., S.Y., Z.W., D.G., X.L., Z.Z., and B.C.; Writing and review: Y.J., J.C., J.G., Y.T., D.C., J.H., Y.S., S.Y., E.-G.W., L.-M.X., and X.-Z.L. **Competing interests:** The authors declare no competing interests. **Data and materials availability:** The tabulated data used to create the Figures for the main text have been deposited in Zenodo (*46*). All other data needed to evaluate the conclusions in the paper are present in the paper or the Supplementary Materials.

SUPPLEMENTARY MATERIALS

science.org/doi/10.1126/science.abo0823
Materials and Methods
Supplementary Text
Figs. S1 to S26
Tables S1 to S3
References (*47*–*74*)

Submitted 12 January 2022; accepted 16 May 2022
10.1126/science.abo0823